

Research Article

Construction of Direct Z-Scheme Photocatalyst by $\text{Mg}_{1.2}\text{Ti}_{1.8}\text{O}_5$ and $\text{g-C}_3\text{N}_4$ Nanosheets toward Photocatalytic H_2 Production and Disinfection

Sijia Gu,¹ Dan Zhang,¹ Shirong Luo,¹ and Heng Yang^{1,2} 

¹Affiliated Huidong Hospital of Guangdong Medical University, Guangdong Medical University, Huizhou 516300, China

²Key Laboratory of Pesticide & Chemical Biology of Ministry of Education, College of Chemistry, Central China Normal University, Wuhan 430070, China

Correspondence should be addressed to Heng Yang; ccnu_yh@sina.com

Received 15 September 2019; Accepted 11 November 2019; Published 1 December 2019

Guest Editor: Muhammad S. Javed

Copyright © 2019 Sijia Gu et al. This is an open access article distributed under the Creative Commons Attribution License, which permits unrestricted use, distribution, and reproduction in any medium, provided the original work is properly cited.

Exploring a novel and efficient photocatalyst is the key research goal to relieve energy and environmental issues. Herein, Z-scheme heterojunction composites were successfully fabricated by loading $\text{g-C}_3\text{N}_4$ nanosheets (CN) on the surface of $\text{Mg}_{1.2}\text{Ti}_{1.8}\text{O}_5$ nanoflakes (MT) through a simple sol-gel method followed by the calcination method. The crystalline phase, morphologies, specific surface area, and optical and electrochemical performance of the samples were characterized by X-ray diffraction (XRD), field emission scanning electron microscopy (FE-SEM), energy-disperse X-ray spectroscopy (EDS), Brunauer-Emmett-Teller (BET), diffuse reflectance spectroscopy (DRS), and electrochemical measurements. Considering the suitable band structures of the components, the photocatalytic performance was evaluated by photocatalytic H_2O splitting and photocatalytic inactivation of *Escherichia coli* (*E. coli*). Among the samples, MT/CN-10 (the molar percentage of melamine to as-obtained Mg-Ti gel was 10%) shows superior photocatalytic performance, which the average H_2 production rate was 3.57 and 7.24 times higher than those of MT and CN alone. Additionally, the efficiency of inactivating *Escherichia coli* (*E. coli*) over MT/CN-10 was 1.95 and 2.06 times higher as compared to pure MT and CN, respectively. The enhancement of the photocatalytic performance was attributed to the advantages of the extremely negative conduction band (CB) of CN and the extremely positive valence band (VB) of MT, the enhanced light absorption, and more efficient photogenerated charge carrier separation.

1. Introduction

During the past decade, there is an increasing interest in addressing the problem related to the growing concentration of energy shortage and other related damaging environmental pollutions due to the combustion of the fossil fuels [1–3]. Under the circumstances, developing advanced technologies is very urgent, which are able to reduce the use of fossil fuels and exploit the renewable and environmentally friendly energy sources [4–6]. Photocatalytic technology is a promising approach towards solving the above problems, which can transform H_2O into H_2 and relieve the environmental pollution under solar light irradiation. Thus, considerable research efforts have been made to develop efficient photocatalysts for the usage of photocatalytic hydrogen production and disin-

fection due to the technology advantage of convenient and environmentally friendly operation process and no harmful disinfection by-products, such as metal oxide and sulfide, as well as metal chloride semiconductors [7–11]. Lately, perovskite as a semiconductor photocatalyst for water splitting has become a research hotspot. Compared with the most studied metal oxides and sulfides, the perovskite shows a more suitable conduction band position and higher stability, as well as abundant light absorption. Magnesium titanate, as a member of the perovskite family, has been reported to be an efficient photocatalyst of water splitting to product hydrogen and the degradation of pollutants. However, pure perovskite has two major drawbacks, namely, low surface area and high recombination rate of photogenerated electron hole pairs [12–15]. Therefore, to enhance the photocatalytic efficiency,

the strategy of designing effective artificial photosynthetic systems by mimicking the Z-scheme mechanism in the chloroplast has been developed. Graphitic carbon nitride ($g\text{-C}_3\text{N}_4$), as a metal-free polymeric semiconductor with a narrow bandgap of about 2.7 eV, has been widely studied among various semiconductors in view of its low cost, non-toxicity, good thermal and chemical stability, and higher reduction potential position [16–22]. However, the poor separation efficiency of photogenerated charge carriers and insufficient light absorption of bulk $g\text{-C}_3\text{N}_4$ directly synthesized by the thermal polycondensation method would lead to inferior performance and limitation of application [23–28]. Given that of these shortcomings, constructing the Z-scheme heterostructure by recombining $g\text{-C}_3\text{N}_4$ with perovskite has been regarded as an ideal solution to expand the specific surface area and restrain the recombination of photogenerated charges.

Herein, we have successfully synthesized the Z-scheme heterojunction photocatalyst consisting of $\text{Mg}_{1.2}\text{Ti}_{1.8}\text{O}_5$ nanosheets (MT) and $g\text{-C}_3\text{N}_4$ nanosheets (CN) by the sol-gel method and calcination method. The photocatalytic performance was evaluated by photocatalytic water splitting and disinfection under simulated sunlight irradiations. Compared with pure $\text{Mg}_{1.2}\text{Ti}_{1.8}\text{O}_5$ and $g\text{-C}_3\text{N}_4$, the Z-scheme heterojunction photocatalyst exhibited excellent photocatalytic activity by taking the advantages of the more negative conduction band (CB) of CN, the more positive valence band (VB) of MT, the enhanced light absorption, and more efficient photogenerated charge carrier separation.

2. Experimental Section

2.1. The Preparation of Photocatalyst. All chemicals used in this work were analytical grade without any further purification. The heterojunction composite composed of $g\text{-C}_3\text{N}_4$ and $\text{Mg}_{1.2}\text{Ti}_{1.8}\text{O}_5$ was obtained by the sol-gel method and ionothermal method. In a typical sol-gel preparation procedure, 0.03 mol of acetic acid was poured into 0.16 mol absolute ethanol to form a transparent solution, and then 0.01 mol of $\text{Ti}(\text{OC}_4\text{H}_9)_4$ was dropped into the above solution with constantly stirring to form transparent solution. After that, 0.01 mol of $\text{Mg}(\text{NO}_3)_2 \cdot 6\text{H}_2\text{O}$ was slowly added into the above solution to generate homogeneous yellow sol. Finally, the above yellow sol was dried in air to obtain Mg-Ti gel. Additionally, in the process of ionothermal calcination method, a certain amount of melamine was mixed with the as-obtained Mg-Ti gel at molar ratio of 5%, 10%, and 20%, respectively. Then, the above mixture (1.0 g) was mixed with KCl (2.75 g) and LiCl (2.25 g). After being mixed evenly, the resultant mixture was transferred into a corundum crucible and calcined at 550°C for 2 h with a heating rate of 5°C/min in a muffle furnace. The resultant product was washed with boiling distilled water and then followed by drying at 60°C overnight in a vacuum oven. By way of comparison, pure $g\text{-C}_3\text{N}_4$ and $\text{Mg}_{1.2}\text{Ti}_{1.8}\text{O}_5$ were also prepared using the similar procedure. The synthetic samples were labeled as CN, MT, MT/CN-5, MT/CN-10, and MT/CN-20, respectively.

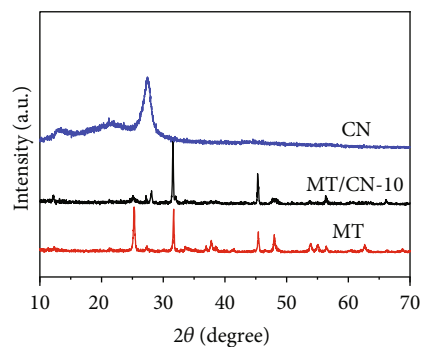


FIGURE 1: XRD patterns of pure CN, MT, and MT/CN-10 Z-scheme heterojunction photocatalyst.

2.2. Characterizations. The X-ray diffraction (XRD) patterns were recorded on a Bruker D8 Advance instrument with $\text{Cu-K}\alpha$ as the radiation source. The morphologies of the as-obtained samples were characterized by a JSM-7500 field emission scanning electron microscope (FE-SEM). The specific surface area and pore structure were analyzed by N_2 adsorption-desorption isotherms using a Micromeritics ASAP 2020 Apparatus (Micromeritics Instruments, USA). The optical performance of samples was characterized by a UV-visible spectrophotometer (UV-2600, Shimadzu, Japan). Room temperature photoluminescence (PL) emission spectra of the samples were collected on a Hitachi F-700 fluorescence spectrophotometer at an excitation wavelength of 325 nm. Electrochemical measurements were carried out on an electrochemical workstation (CHI66E, China) with a standard three-electrode cell, where Na_2SO_4 solution as the electrolyte, Pt foil acted as the counter electrode, and Ag/AgCl (saturated KCl) as the reference electrode.

2.3. Evaluation of Photocatalytic Hydrogen Evolution. The photocatalytic hydrogen evolution was evaluated on a Labsolar-6A system (Pefect Light Company, Beijing China), where a 300 W Xenon arc lamp was used as simulated sunlight source. In the process of photocatalytic water splitting, circulating cooling water system is used to guarantee that the temperature of reaction system be kept at $25 \pm 1^\circ\text{C}$. Firstly, 50 mg of the as-prepared photocatalyst was dispersed in 80 ml of triethanolamine (TEOA) aqueous solution (10 vol%). Then, a certain amount of H_2PtCl_6 aqueous solution was dripped into the system to load 1.0 wt% Pt onto the surface of the photocatalyst by a photochemical reduction deposition method. After illumination for 1 h under magnetic stir, 0.4 ml of the produced gas was automatically withdrawn and injected into the gas chromatograph (GC-2014C, Shimadzu, Japan) to determine the concentration of the produced H_2 gas.

2.4. Photocatalytic Disinfection Experiment. The photocatalytic performance of the obtained samples was evaluated by the inactivation of *Escherichia coli* (*E. coli*). Firstly, in order to obtain the inoculum, the bacteria was incubated in 100 ml Luria-Bertani (LB) nutrient solution and shaken at 37°C for 12 h, and then centrifuged to remove the metabolites.

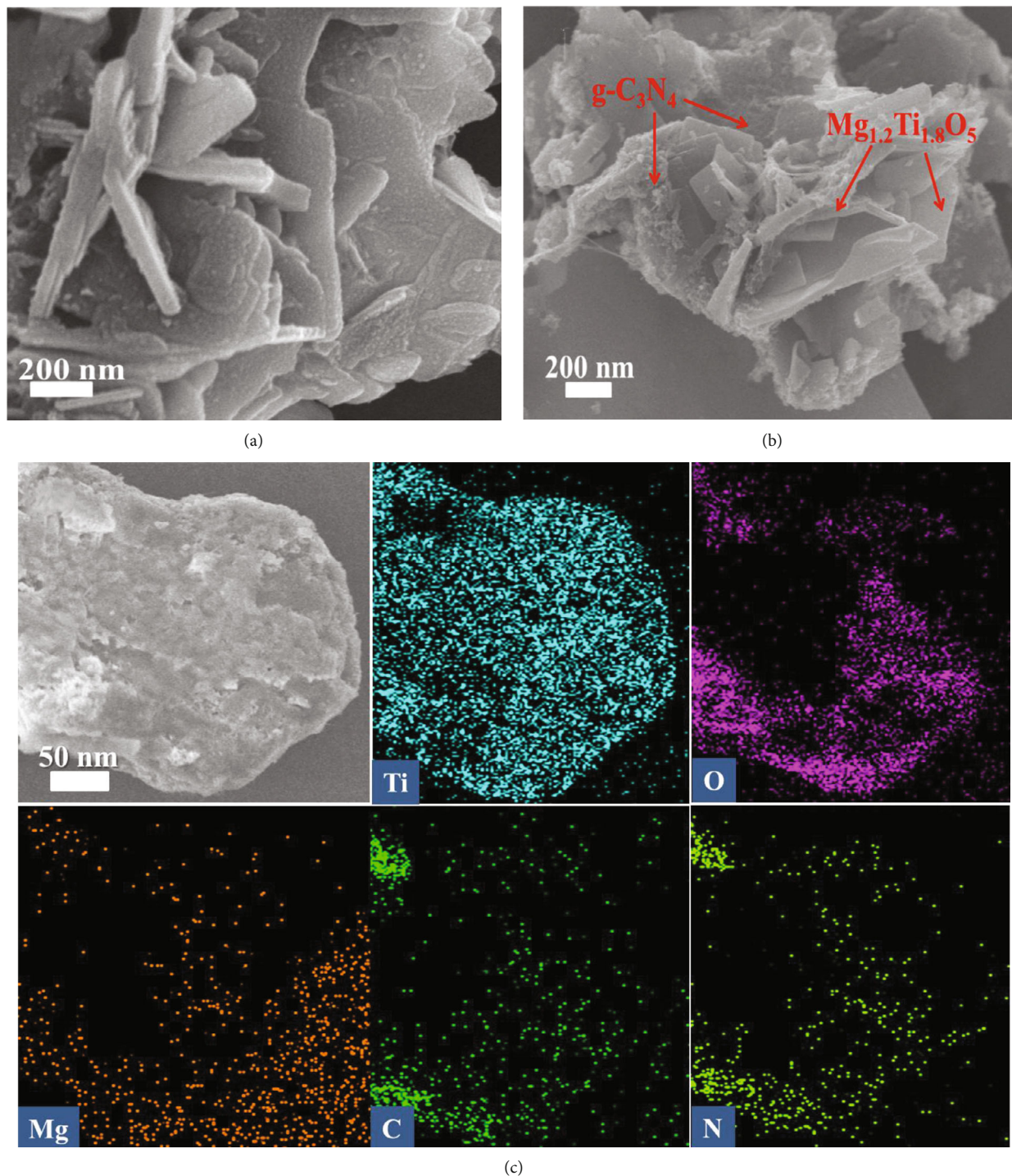


FIGURE 2: (a) FE-SEM images of pure MT. (b) MT/CN heterojunction. (c) SEM-EDS element mapping analysis of the MT/CN heterojunction.

Subsequently, the bacterial cell pellet was washed twice with sterilized saline (0.9% NaCl) solution and then resuspended in the sterilized saline solution. The obtained bacteria cell density was about 5×10^7 colony forming units per milliliter (CFU/ml). Finally, the photocatalytic disinfection experiment was carried out. Namely, 30 ml of *E. coli* suspension was mixed with 20 mg photocatalyst powder and stirred at 500 rpm for 5 min in the dark. A 300 W Xenon lamp with

an AM1.5 filter was employed as the simulated sunlight source to irradiate the *E. coli* cells. At regular intervals, aliquots were taken from the suspension buffer and 0.1 ml of the suspension (undiluted, three replicates) was spread onto LB agar plates, and then incubated at 37°C for 18 h to form viable colony units. All inactivation experiments were performed in triplicate, and all glassware was heated at 120°C for 20 min in an autoclave to ensure the sterility.

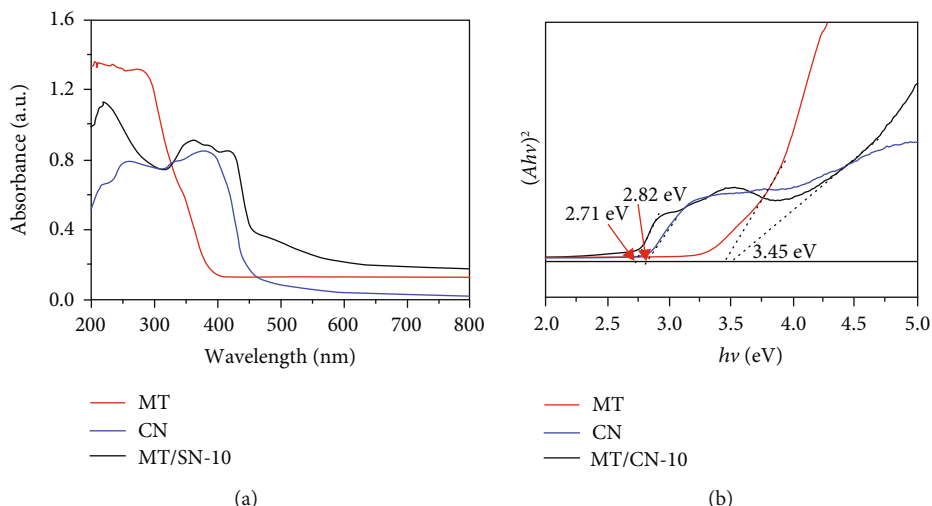


FIGURE 3: (a) UV-Vis absorption spectra and (b) the bandgap evaluation from the $(\alpha h\nu)$ [2] photon energy plots for CN, MT/CN-10, and MT samples.

3. Results and Discussion

The XRD patterns of the synthesized CN, MT, and MT/CN-10 composite are shown in Figure 1. It can be observed that the two typical diffraction peaks of CN appeared at 27.5° and 13.1° are classified to (002) and (100) diffraction planes, which are assigned to the interlayer stacking of aromatic segments and in-plane structural packing motif of tri-s-triazine units [29–31]. The pure MT exhibits five stronger diffraction peaks at 2θ of 25.5° , 32.1° , 39.6° , 45.4° , and 48.2° , corresponding to the (110), (023), (113), (043), and (200) facets, respectively [12]. After the introduction of CN into the MT, the heterojunction sample reveals characteristic diffraction peaks for both CN and MT without any position shifts, indicating the coexistence of these two components in the heterojunctions.

The field emission scanning electron microscope (FE-SEM) measurement was carried out to characterize the morphologies and structures of MT and MT/CN samples. As shown in Figure 2(a), the pristine MT displays the aggregated structure consisting of several two-dimensional (2D) sheets with a thickness of 10–20 nm. By contrast, the image of MT/CN composite shows that many CN nanoparticles grow on the surface of the 2D MT nanosheets (Figure 2(b)). The microstructure of the MT/CN composite was further explored by SEM-EDS elemental mapping measure. The elemental mapping images reveal C, N, Ti, and O, and Mg elements are well-distributed in the composite (Figure 2(c)). Those abovementioned results further proved that the MT/CN heterojunction was successfully synthesized.

The optical absorption properties of the obtained samples were investigated by UV-vis diffuse reflectance measurement. As shown in Figure 3(a), steep adsorption band edge of pure MT is observed in the ultraviolet region, whereas an obvious adsorption edge which can be assigned to the intrinsic bandgap absorption of pure CN is approximately located at 450 nm. Remarkably, the adsorption band edge of the MT/CN-10 heterojunction photocatalyst exhibits a red shift in comparison to that of pristine CN and MT, implying that

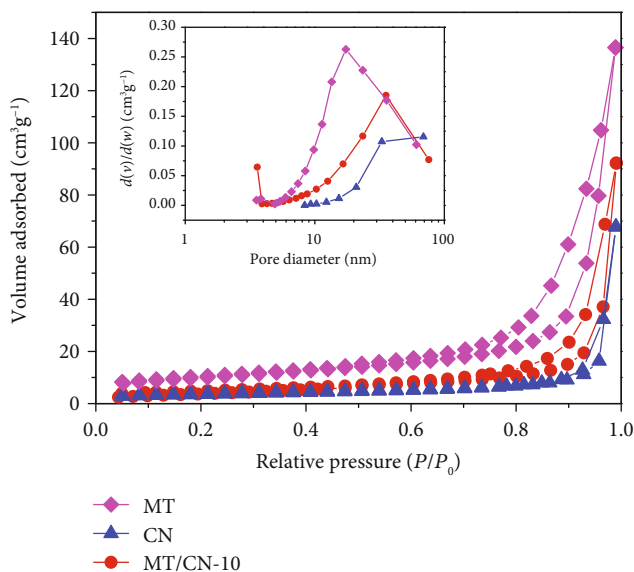


FIGURE 4: The N₂ adsorption-desorption isotherms and pore size distributions (inset of the figure).

TABLE 1: Physicochemical properties of MT, CN, and MT/CN-10 composite.

Sample	S_{BET} (m ² g ⁻¹)	Cumulative volume of pores (cm ³ g ⁻¹)	Average pore diameter (nm)
MT	34.7	0.21	24.1
CN	12.1	0.10	34.4
MT/CN-10	20.9	0.15	31.5

the enhanced light absorption ability would be highly conducive to boost the photocatalytic performance. Moreover, the optical bandgap energy can be calculated by the following equation [32, 33]:

$$\alpha h\nu = A(h\nu - E_g)^{n/2}, \quad (1)$$

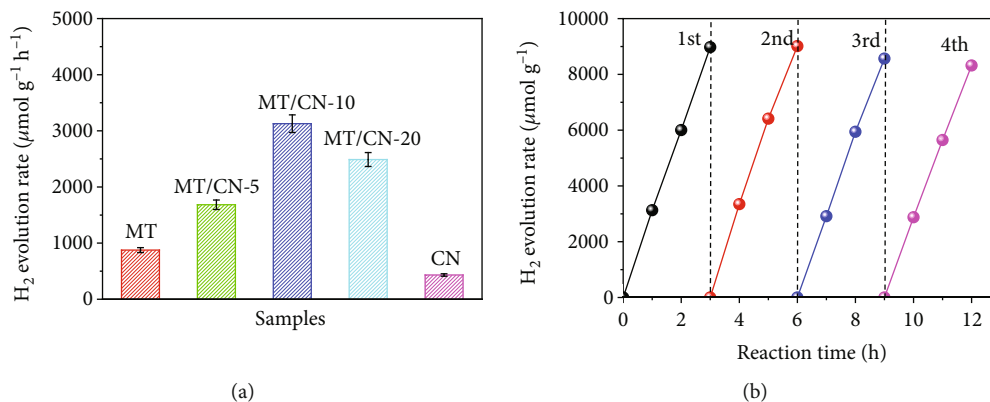
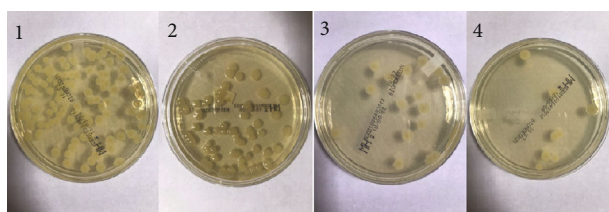
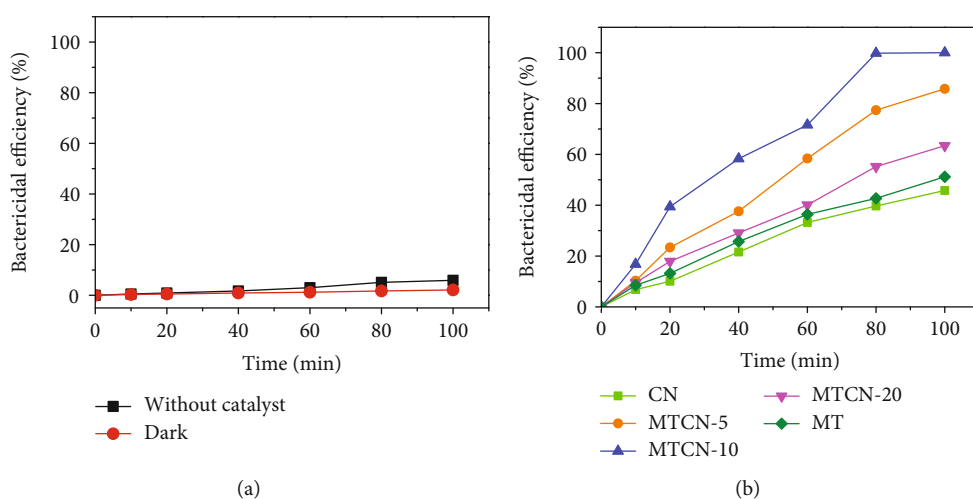


FIGURE 5: (a) Comparison of H₂ generation rate of as-prepared samples under Xenon lamp irradiation (full spectrum), with photodeposition of 1% Pt as cocatalyst. (b) Time courses of photocatalytic H₂ generation amount of MT/CN-10.



(c)

FIGURE 6: (a) Inactivation efficiency against *E. coli* by photocatalyst in the dark and without photocatalyst under simulated solar light. (b) The inactivation of *E. coli* by as-prepared photocatalysts under simulated solar light. (c) Photographs of colonies formed by *E. coli* cells in water samples after treated by MT/CN-10 suspensions with simulated solar light for 0 (c1), 20 (c2), 60 (c3), and 80 (c4) min.

where A , α , $h\nu$, and E_g represent a constant, the absorption coefficient, the photon energy, and the optical bandgap, respectively. In this equation, n is determined by the transition type. The bandgap energies of the MT and CN are determined from a plot of $(\alpha h\nu)^2$ versus $h\nu$ ($n = 1$ for direct transition). Thus, the bandgaps of MT and CN are estimated to 3.45 eV and 2.71 eV, respectively (Figure 3(b)).

The adsorption-desorption curves and pore volume distribution curves of MT, CN, and MT/CN-10 composite are shown in Figure 4. And the corresponding calculated results of BET surface area are also listed in Table 1. Obviously, all samples exhibit the type IV isotherms with type H3 hysteresis loops [34, 35], which are characteristics of slit-like pores

formed by the stacking of nanosheets. However, after combining CN with the MT, the specific surface area and pore volume of MT/CN composite distinctly decreased as compared to that of pure MT, which might attributed to the fact that the small CN nanosheets filled or blocked large numbers of micropores of MT.

The photocatalytic performance of the obtain catalysts was evaluated by photocatalytic hydrogen production under simulated solar light irradiation. Figure 5(a) depicts the photocatalytic H₂ evolution rate of various photocatalysts. The results showed that the H₂ evolution rate firstly increased and then decreased with the increasing loading amount of CN. The MT/CN-10 in particular outperforms (3128.3 μmol/h/g)

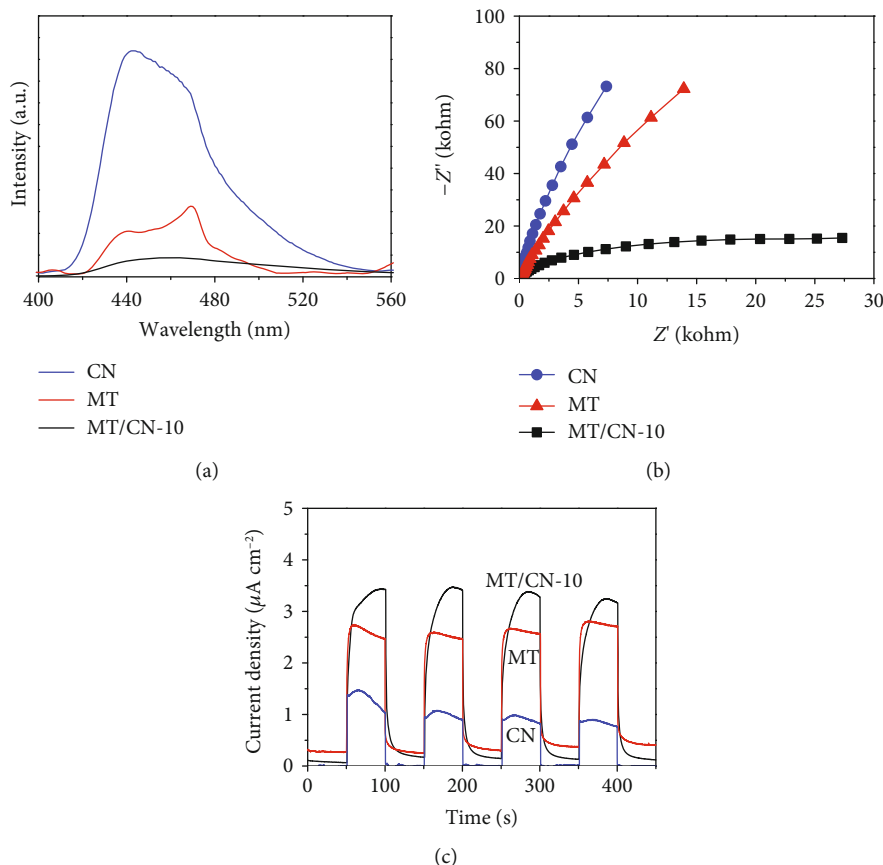


FIGURE 7: (a) Steady-state photoluminescence spectrum (PL) of samples (excitation wavelength of 325 nm). (b) Nyquist plots of electrochemical impedance spectra (EIS) for samples. (c) Transient photocurrent-time profiles for samples.

among all the photocatalysts, which was about 3.57 and 7.24 times higher than that of pure MT and CN, respectively. The stability and reusability of the photocatalyst is of great significance to its practical application. Figure 5(b) demonstrates no significant decrease in the photocatalytic H_2 production amount of MT/CN-10 after four repetitive cycles, indicating that MT/CN-10 possesses high photocatalytic stability and recyclability. Moreover, in order to assess the enhanced photocatalytic efficiency of MT/CN composites, the inactivation efficiencies of the *E. coli* over the as-prepared samples were also investigated in Figure 6. Compare the photocatalytic disinfection efficiencies of different samples under simulated solar light irradiation at room temperature and ambient pressure as well as the blank one with photocatalyst (MT/CN-10 sample alone) but under dark condition. In parallel, the inactivation efficiency of the *E. coli* without adding any photocatalysts was also evaluated. As it can be found in Figure 5(a), the inactivation of the bacteria barely happens in the absence of photocatalyst, and no disinfection efficiency of the *E. coli* was observed when the photocatalyst (MT/CN-10) is used without light irradiation. In addition, the MT/CN composites exhibit higher inactivation efficiencies than that of pure MT and CN by the simulated solar light illumination. Particularly, almost 100.0% of *E. coli* can be killed by MT/CN-10 over 100 min of simulated solar light exposure (Figures 6(b) and 6(c)), while the inactivation efficiencies only reach to 51.2% and 48.5% for pure MT and CN after 100 min, respec-

tively. These results demonstrate that the photocatalytic *E. coli* inactivation activity can be significantly improved by constructing the heterojunction about CN and MT.

To reveal the significant effect of CN on the photocatalytic activity of MT, the photoluminescence (PL), photocurrent responses, and electrochemical impedance spectrum (EIS) analysis were conducted to explore the charge carrier transfer efficiencies of pure MT, CN, and MT/CN-10 composite. Figure 7(a) shows that the PL intensity of MT/CN-10 is the weakest than that of pure MT and CN, and the CN displays the strongest PL intensity, indicating that the recombination of photogenerated charge carriers is effectively inhibited after loading CN on the surface of MT. Furthermore, the enhanced transport of charge carriers can be further evidenced by the lower electric resistance and higher photocurrent response. As shown in Figure 7(b), the MT/CN-10 composite exhibits the smallest semicircle. And the MT/CN-10 hybrid can afford a much enhanced current density than that of the bare MT and CN (Figure 7(c)). These above results further corroborate that the heterojunction between MT and CN can enhance the separation and transfer efficiency of charge carriers, which is beneficial for improving the photocatalytic disinfection performance.

The electronic spin resonance (ESR) measurement was carried out to detect the active radicals [36, 37]. As displayed in Figure 8(a), the DMPO- $\cdot\text{OH}$ signal can be observed for pure MT and MT/CN-10, while no DMPO- $\cdot\text{OH}$ signal is

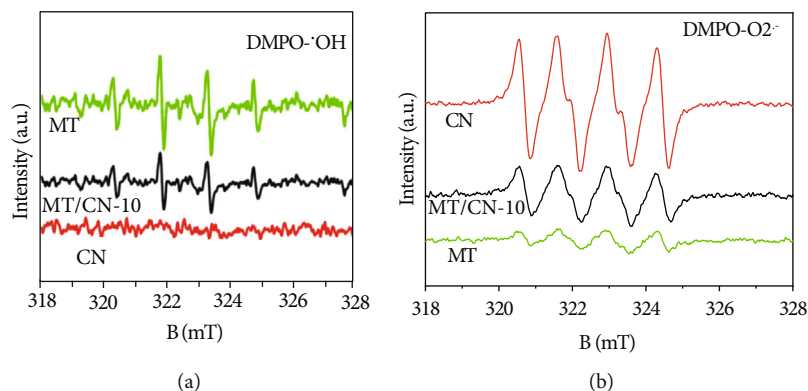


FIGURE 8: The DMPO spin-trapping ESR spectrum for (a) DMPO·OH and (b) DMPO·O₂⁻ under simulated solar light irradiation.

found for pure CN; this is due to the weak oxidation potential of CN. The strongest DMPO·OH signal for MT/CN-10 suggests that the photogenerated holes still stay in the valence band (VB). At the same time, the DMPO·O₂⁻ signals can be also observed for pure CN and MT/CN-10, but weak DMPO·O₂⁻ signal appears in the MT (Figure 8(b)). The results indicate that the photogenerated electrons and holes stay in the conduction band (CB) of CN and the valence band (VB) of MT, respectively. The conventional type II heterojunction mechanism is hard to explain the EPR results. Contrarily, the Z-scheme heterojunction mechanism is more reasonable to explain the enhancement of the photocatalytic H₂ production and disinfection performance.

According to the atom's Mulliken electronegativity definition formula (Equations (2) and (3)) [38, 39],

$$E_{VB} = X - E_0 + 0.5E_g, \quad (2)$$

$$E_{CB} = E_{VB} - E_g, \quad (3)$$

where E_{VB} is the valence band potential, E_{CB} is the conduction band potential, E_g is the semiconductor bandgap energy, E_0 is the electron free energy (in general 4.5 eV), and X is the geometrical mean of the absolute electronegativity of each atom in the semiconductor. Thus, the E_{VB} and E_{CB} of MT are 3.11 V and -0.34 V, whereas the E_{VB} and E_{CB} of CN are 1.59 V and -1.12 V, respectively. To the end, the mechanism of the enhanced disinfection performance for the MT/CN heterojunction composites under simulated solar light irradiation is shown in Figure 9. Under simulated solar light irradiation, the excited electrons transfer from the CB of CN to the CB of MT, and the excited holes transfer from the VB of MT to the VB of CN. Thus, an internal electric field is produced at the interface between CN and MT. Simultaneously, band edge of CN bends upward due to the loss of electrons, but band edge of MT bends downward due to the accumulation of electrons. Under the influence of the internal electric field, the electrons on the CB of MT transfer to the VB of CN and recombine with the holes on the VB of CN. Therefore, more electron hole pairs can be efficiently separated, and more electrons and active radicals are obtained to enhance the photocatalytic H₂ production and disinfection, respectively.

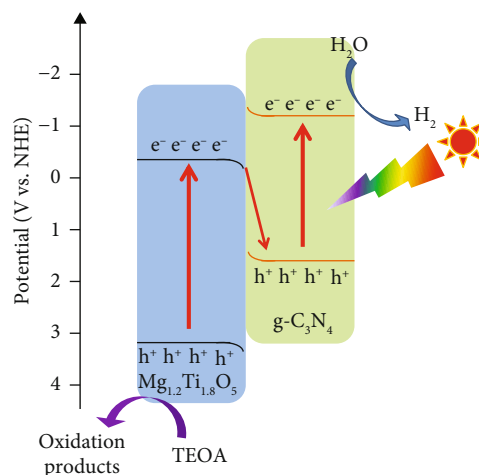


FIGURE 9: A possible photocatalytic mechanism for H₂ production based on MT/CN heterostructure.

4. Conclusions

In this work, we successfully synthesized a Z-scheme 2D/2D MT/CN heterostructured photocatalyst by a simple sol-gel method followed by calcination method to grow CN nanosheets on the surface of MT nanoflakes. And the MT/CN-10 exhibited much more excellent photocatalytic H₂ production performance and disinfection efficiency than that of pure MT and CN. The establishment of heterojunction between MT and CN can lead a superior interfacial charge transfer under simulated solar light irradiation so as to generate more electrons and active radicals for H₂ production and bacteria inactivation, respectively. In addition, the efficient harvesting of light and the large specific surface area of 2D MT/CN nanosheets are of great importance of the enhancement of the photocatalytic efficiency. These results could provide a new view for the design of heterojunction photocatalysts for applications in solar-to-chemical energy conversion and environmental remediation.

Data Availability

The data used to support the findings of this study are available from the corresponding author upon request.

Conflicts of Interest

The authors declare that there is no conflict of interests regarding the publication of this paper.

Authors' Contributions

Dan Zhang and Shirong Luo contributed equally to this work.

Acknowledgments

This work was supported by the Science and Technology Planning Project of Huizhou (2018Y322).

References

- [1] Q. Liu, Y. Xu, J. Wang et al., "Fabrication of Ag/AgCl/ZnFe₂O₄ composites with enhanced photocatalytic activity for pollutant degradation and *E. coli* disinfection," *Colloids and Surfaces A: Physicochemical and Engineering Aspects*, vol. 553, no. 20, pp. 114–124, 2018.
- [2] M. Mousavi, A. Habibi-Yangjeh, and S. R. Pouran, "Review on magnetically separable graphitic carbon nitride-based nanocomposites as promising visible-light-driven photocatalysts," *Journal of Materials Science: Materials in Electronics*, vol. 29, no. 3, pp. 1719–1747, 2018.
- [3] Z. G. Zhao and M. Miyauchi, "Nanoporous-walled tungsten oxide nanotubes as highly active Visible-Light-Driven photocatalysts," *Angewandte Chemie International Edition*, vol. 47, no. 37, pp. 7051–7055, 2008.
- [4] R. P. Schwarzenbach, B. I. Escher, K. Fenner et al., "The challenge of micropollutants in aquatic systems," *Science*, vol. 313, no. 5790, pp. 1072–1077, 2006.
- [5] D. L. Sedlak and U. von Gunten, "The chlorine dilemma," *Science*, vol. 331, no. 6013, pp. 42–43, 2011.
- [6] X. Zeng, Z. Wang, G. Wang et al., "Highly dispersed TiO₂ nanocrystals and WO₃ nanorods on reduced graphene oxide: Z-scheme photocatalysis system for accelerated photocatalytic water disinfection," *Applied Catalysis B: Environmental*, vol. 218, no. 5, pp. 163–173, 2017.
- [7] M. Pelaez, N. T. Nolan, S. C. Pillai et al., "A review on the visible light active titanium dioxide photocatalysts for environmental applications," *Applied Catalysis B: Environmental*, vol. 125, no. 21, pp. 331–349, 2012.
- [8] M. D. Hernández-Alonso, F. Fresno, S. Suárez, and J. M. Coronado, "Development of alternative photocatalysts to TiO₂: challenges and opportunities," *Energy & Environmental Science*, vol. 2, no. 12, pp. 1231–1257, 2009.
- [9] C. A. Castro, A. Jurado, D. Sissa, and S. A. Giraldo, "Performance of Ag-TiO₂ photocatalysts towards the photocatalytic disinfection of water under interior lighting and solar simulated light irradiations," *International Journal of Photoenergy*, vol. 2012, Article ID 261045, pp. 1–10, 2012.
- [10] Q. Zhou, S. Ma, and S. Zhan, "Superior photocatalytic disinfection effect of Ag-3D ordered mesoporous CeO₂ under visible light," *Applied Catalysis B: Environmental*, vol. 224, no. 4, pp. 27–37, 2018.
- [11] Y. Jia, S. Zhan, S. Ma, and Q. Zhou, "Fabrication of TiO₂-Bi₂WO₆ nanosheet for enhanced solar photocatalytic disinfection of *E. coli*: insights on the mechanism," *ACS Applied Materials & Interfaces*, vol. 8, no. 11, pp. 6841–6851, 2016.
- [12] N. Zhang, Y. Qu, K. Pan, G. Wang, and Y. Li, "Synthesis of pure phase Mg_{1.2}Ti_{1.8}O₅ and MgTiO₃ nanocrystals for photocatalytic hydrogen production," *Nano Research*, vol. 9, no. 3, pp. 726–734, 2016.
- [13] L. Meng, Z. Ren, W. Zhou, Y. Qu, and G. Wang, "MgTiO₃/Mg-Ti₂O₅/TiO₂ heterogeneous belt-junctions with high photocatalytic hydrogen production activity," *Nano Research*, vol. 10, no. 1, pp. 295–304, 2017.
- [14] Y. Qu, W. Zhou, Y. Xie et al., "A novel phase-mixed MgTiO₃-MgTi₂O₅ heterogeneous nanorod for high efficiency photocatalytic hydrogen production," *Chemical Communications*, vol. 49, no. 76, pp. 8510–8512, 2013.
- [15] X. Zhou, J. Yao, M. Yang et al., "Synthesis of MoSe₂/SrTiO₃-Heterostructures with enhanced ultraviolet-light-driven and visible-light-driven photocatalytic properties," *Nano*, vol. 13, no. 04, p. 1850038, 2018.
- [16] J. Xu, Q. Gao, X. Bai, Z. Wang, and Y. Zhu, "Enhanced visible-light-induced photocatalytic degradation and disinfection activities of oxidized porous g-C₃N₄ by loading Ag nanoparticles," *Catalysis Today*, vol. 332, no. 34, pp. 227–235, 2019.
- [17] W. Ong, L. Tan, Y. Ng, S. Yong, and S. Chai, "Graphitic carbon nitride (g-C₃N₄)-based photocatalysts for artificial photosynthesis and environmental remediation: are we a step closer to achieving sustainability?," *Chemical Reviews*, vol. 116, no. 12, pp. 7159–7329, 2016.
- [18] G. Mamba and A. K. Mishra, "Graphitic carbon nitride (g-C₃N₄) nanocomposites: a new and exciting generation of visible light driven photocatalysts for environmental pollution remediation," *Applied Catalysis B: Environmental*, vol. 198, no. 5, pp. 347–377, 2016.
- [19] Y. Zheng, L. Lin, B. Wang, and X. Wang, "Graphitic carbon nitride polymers toward sustainable photoredox catalysis," *Angewandte Chemie International Edition*, vol. 54, no. 44, pp. 12868–12884, 2015.
- [20] Y. Wang, X. Wang, and M. Antonietti, "Polymeric graphitic carbon nitride as a heterogeneous organocatalyst: from photochemistry to multipurpose catalysis to sustainable chemistry," *Angewandte Chemie International Edition*, vol. 51, no. 1, pp. 68–89, 2012.
- [21] S. Cao, J. Low, J. Yu, and M. Jaroniec, "Polymeric photocatalysts based on graphitic carbon nitride," *Advanced Materials*, vol. 27, no. 13, pp. 2150–2176, 2015.
- [22] K. Liu, J. Li, X. Yan, and W. Shi, "Synthesis of Direct Z-Scheme MnWO₄/g-C₃N₄ Photocatalyst with enhanced visible light photocatalytic activity," *Nano*, vol. 12, no. 10, p. 1750129, 2017.
- [23] J. Xu, Z. Wang, and Y. Zhu, "Enhanced visible-light-driven photocatalytic disinfection performance and organic pollutant degradation activity of porous g-C₃N₄ nanosheets," *ACS Applied Materials & Interfaces*, vol. 9, no. 33, pp. 27727–27735, 2017.
- [24] M. Wu, J. Yan, X. Tang, M. Zhao, and Q. Jiang, "Synthesis of potassium-modified graphitic carbon nitride with high photocatalytic activity for hydrogen evolution," *ChemSusChem*, vol. 7, no. 9, pp. 2654–2658, 2014.
- [25] S. Fang, Y. Xia, K. Lv, Q. Li, J. Sun, and M. Li, "Effect of carbon dots modification on the structure and photocatalytic activity of g-C₃N₄," *Applied Catalysis B: Environmental*, vol. 185, no. 15, pp. 225–232, 2016.
- [26] G. Liao, S. Chen, X. Quan, H. Yu, and H. Zhao, "Graphene oxide modified g-C₃N₄ hybrid with enhanced photocatalytic

- capability under visible light irradiation,” *Journal of Materials Chemistry*, vol. 22, no. 6, pp. 2721–2726, 2012.
- [27] H. Bian, Y. Ji, J. Yan et al., “In situ synthesis of few-layered g-C₃N₄ with vertically aligned MoS₂ loading for boosting solar-to-hydrogen generation,” *Small*, vol. 14, no. 3, p. 1703003, 2018.
- [28] P. Niu, L. Zhang, G. Liu, and H. M. Cheng, “Graphene-like carbon nitride nanosheets for improved photocatalytic activities,” *Advanced Functional Materials*, vol. 22, no. 22, pp. 4763–4770, 2012.
- [29] Y. N. Li, Z. Y. Chen, M. Q. Wang, L. Z. Zhang, and S. J. Bao, “Interface engineered construction of porous g-C₃N₄/TiO₂ heterostructure for enhanced photocatalysis of organic pollutants,” *Applied Surface Science*, vol. 440, no. 15, pp. 229–236, 2018.
- [30] J. Fu, B. Zhu, C. Jiang, B. Cheng, W. You, and J. Yu, “Hierarchical porous O-doped g-C₃N₄ with enhanced photocatalytic CO₂ reduction activity,” *Small*, vol. 13, no. 15, p. 1603938, 2017.
- [31] Y. Xia, Z. He, J. Su, Y. Liu, B. Tang, and X. Li, “Fabrication of novel n-SrTiO₃/p-BiOI heterojunction for degradation of crystal violet under simulated solar light irradiation,” *Nano*, vol. 13, no. 06, p. 1850070, 2018.
- [32] S. Zhou, J. Huang, T. Zhang, H. Ouyang, A. Li, and Z. Zhang, “Effect of variation Mn/W molar ratios on phase composition, morphology and optical properties of MnWO₄,” *Ceramics International*, vol. 39, no. 5, pp. 5159–5163, 2013.
- [33] X. Liu, A. Jin, Y. Jia et al., “Synergy of adsorption and visible-light photocatalytic degradation of methylene blue by a bifunctional Z-scheme heterojunction of WO₃/g-C₃N₄,” *Applied Surface Science*, vol. 405, no. 31, pp. 359–371, 2017.
- [34] Q. Liang, Z. Li, Y. Bai, Z. H. Huang, F. Kang, and Q. H. Yang, “A composite polymeric carbon nitride with in situ formed isotype heterojunctions for highly improved photocatalysis under visible light,” *Small*, vol. 13, no. 9, p. 1603182, 2017.
- [35] S. Ma, S. Zhan, Y. Jia, Q. Shi, and Q. Zhou, “Enhanced disinfection application of Ag-modified g-C₃N₄ composite under visible light,” *Applied Catalysis B: Environmental*, vol. 186, no. 5, pp. 77–87, 2016.
- [36] D. Spasiano, R. Marotta, I. Gargano et al., “Kinetic modeling of partial oxidation of benzyl alcohol in water by means of Fe(III)/O₂/UV-solar simulated process,” *Chemical Engineering Journal*, vol. 249, no. 1, pp. 130–142, 2014.
- [37] Q. Zhao, X. Liu, Y. Xing, Z. Liu, and C. Du, “Synthesizing Bi₂O₃/BiOCl heterojunctions by partial conversion of BiOCl,” *Journal of Materials Science*, vol. 52, no. 4, pp. 2117–2130, 2017.
- [38] N. Li, H. Teng, L. Zhang, J. Zhou, and M. Liu, “Synthesis of Mo-doped WO₃ nanosheets with enhanced visible-light-driven photocatalytic properties,” *RSC Advances*, vol. 5, no. 115, pp. 95394–95400, 2015.
- [39] X. Bai, L. Wang, R. Zong, and Y. Zhu, “Photocatalytic activity enhanced via g-C₃N₄ nanoplates to nanorods,” *Journal of Physical Chemistry C*, vol. 117, no. 19, pp. 9952–9961, 2013.



Hindawi

Submit your manuscripts at
www.hindawi.com

